Xing Liu[1]
School of Engineering,
Brown University,
Providence, RI 02912;
George W. Woodruff School of Mechanical
Engineering,
Georgia Institute of Technology,
Atlanta, GA 30332
e-mail: xing.liu@me.gatech.edu

Christos E. Athanasiou
School of Engineering,
Brown University,
Providence, RI 02912;
Daniel Guggenheim School of Aerospace
Engineering,
Georgia Institute of Technology,
Atlanta, GA 30332
e-mail: athanasiou@gatech.edu

Cristina López-Pernía
School of Engineering,
Brown University,
Providence, RI 02912
e-mail: cristina_lopez_pernia@brown.edu

Ting Zhu
George W. Woodruff School of Mechanical
Engineering,
Georgia Institute of Technology,
Atlanta, GA 30332
e-mail: ting.zhu@me.gatech.edu

Nitin P. Padture
School of Engineering,
Brown University,
Providence, RI 02912
e-mail: nitin_padture@brown.edu

Brian W. Sheldon[1]
School of Engineering,
Brown University,
Providence, RI 02912
e-mail: brian_sheldon@brown.edu

Tailoring the Toughening Effects in Two-Dimensional Nanomaterial-Reinforced Ceramic Matrix Composites

Ceramic matrix composites (CMCs) reinforced by two-dimensional (2D) nanomaterials have shown extraordinary load-carrying capacities, even in the harsh environments required by emerging applications. Their exceptional mechanical performance, especially fracture toughness, primarily arises from their heterogeneous microstructures. The deliberate dispersion of 2D reinforcements enables toughening mechanisms that are extrinsic to the matrix and thus endows the composites with substantial resistance to catastrophic failure. However, the incomplete understanding of the fracture behavior of such nanocomposites, especially the complex energy dissipation process of the matrix/reinforcement interface, limits the development of stronger and tougher CMCs. To overcome these limitations, we investigate crack deflection and energy dissipation in nanocomposites using an extended cohesive shear-lag model. This new model accounts for interfacial debonding and friction, which critically control the toughening of nanocomposites. Our analysis provides mechanistic insights for optimizing the toughening effects of CMCs. [DOI: 10.1115/1.4063029]

Keywords: fracture toughness, 2D nanomaterials, ceramic matrix composites, failure criteria, mechanical properties of materials, micromechanics

Huajian Gao[1]
School of Engineering,
Brown University,
Providence, RI 02912;
School of Mechanical and Aerospace Engineering,
College of Engineering,
Nanyang Technological University,
Singapore 639798;
Institute of High Performance Computing,
A*STAR,
Singapore 138632
e-mail: huajian.gao@ntu.edu.sg

1 Introduction

Microstructural heterogeneity is a prevalent yet crucial characteristic of both natural and engineered materials. Through sophisticated control of their heterogeneous microstructures, both natural and engineered materials can achieve exceptional mechanical properties and functionalities that are typically superior over those of their individual components [1–5]. A well-known example is high-performance ceramic matrix composites (CMCs), which have drawn much research interest due to their potential applications in harsh environments, i.e., extraordinary load-carrying capacities in high-temperature and chemically aggressive environments similar to those found in space and energy storage systems [6,7]. Such materials possess a unique heterogeneous microstructure that comprises a fine dispersion of reinforcements in the ceramic matrix. These reinforcements enable toughening mechanisms that are extrinsic to the ceramic matrix and thereby endow the composites with sufficient resistance to catastrophic failure under various operating conditions [8]. By contrast, monolithic ceramics are usually plagued by their poor fracture toughness and thus can hardly serve as reliable structural materials. As a result, tailoring the toughening effects is a major objective in the design of CMCs [9–11].

From the microstructural perspective, the toughening effects in CMCs should generally depend on three factors. The first factor is the choice of matrix materials and reinforcements. The typical chemical compositions that are often selected include carbon (C), silicon carbide (SiC), silicon nitride (Si_3N_4), aluminum oxide (Al_2O_3), and the shapes of reinforcements include particles, short fibers, long fibers, and sheets. The second factor is the arrangement of reinforcements in the matrix. The distribution of reinforcements can be either homogeneous or inhomogeneous and their orientation can be aligned or random. The third factor is the interface between the reinforcements and the matrix. The matrix/reinforcement interface may exhibit distinct mechanical properties, depending on the chemical composition and fabrication process of CMCs. Therefore, there is a large design space for tuning the toughening effects in CMCs. All the aforementioned factors have been experimentally studied in the past, at least at a lab scale. Recently, the use of nanomaterials in composites brings in a new factor, i.e., downsizing of reinforcements, which has not been extensively explored but may serve as a potential means to enhance the toughening effects in CMCs [4,12–14].

In this work, we study the mechanics of microfiber-reinforced composites [8] by focusing on the 2D nanomaterial-reinforced composites as a downsized example of microfiber-reinforced composites. We show that the current understanding of the fracture behavior of these 2D nanomaterial-reinforced composites is incomplete, particularly regarding the conditions for crack deflection and the predictions for reinforcement-induced toughening. Fundamental studies of these two aspects are essential to fully harness the benefits of nano-sized reinforcements in future studies. Furthermore, we analyze the key features of 2D nanomaterials (e.g., graphene, reduced graphene oxide, hexagonal boron nitride platelets) that make them unique reinforcements. Finally, we provide general guidelines for optimizing the fracture toughness of 2D nanomaterial-reinforced ceramic composites.

Table 1   Models of initiation of interfacial failure in the literature

Authors		Model geometry		Fracture criteria
Cook and Gordon [19]	An elliptical crack	Approaching a perfect bi-material interface	At normal incidence	Stress ratio
Lee et al. [20]	A sharp crack	Approaching a bi-material interface with pre-existing defects	At normal incidence	Energy release rate ratio
Paggi and Reinoso [31]	A sharp crack	Approaching a bi-material interface with pre-existing defects	At normal incidence	Energy release rate ratio and cohesive law
Martin et al. [34]	A sharp crack	Approaching/impinging on a perfect bi-material interface	At normal incidence	Energetic incremental condition
Kendall [35], Thouless and Evans [36], Ye et al. [37], Gupta et al. [38], Tullock et al. [39], Martínez and Gupta [40], Tu et al. [21], Ahn et al. [22], Leguillon et al. [23], Roham et al. [24], Lee et al. [25]	A sharp crack	Impinging on a perfect bi-material interface	At normal incidence	Energy release rate ratio
Gupta et al. [26,38]	A sharp crack	Impinging on a perfect bi-material interface	At normal incidence	Stress ratio
Parmigiani and Thouless [27]	A sharp crack	Impinging on a perfect bi-material interface	At normal incidence	Cohesive law
He et al. [28–30,32], Leguillon et al. [23], Zhang et al. [33]	A sharp crack	Impinging on a perfect bi-material interface	At oblique incidence	Energy release rate ratio

2 From Fiber-Reinforced Composites to 2D Nanomaterial-Reinforced Composites

2.1 Toughening in Fiber-Reinforced Composites. The investigation of fracture in fiber-reinforced composites can be traced back to the 1960s when the principles of fracture mechanics in homogeneous brittle materials were already well established [15–17]. Over the years, tremendous efforts have been devoted to understanding how a composite material is toughened by embedded fibers, particularly concerning two fundamental questions: (1) what failure mode is enabled in the vicinity of a fiber reinforcement and (2) how to predict the contribution of reinforcements to fracture toughness? Here, we focus on the specific combination of a brittle matrix and brittle fiber reinforcements, as it is most relevant to CMCs.

Regarding the first question, the scenario of a major matrix crack running into an array of fiber reinforcements has been extensively studied in the literature [8]. As pointed out by Cottrell [18], a weak matrix/reinforcement interface, perpendicular to the crack, is the best obstacle to a running crack. Specifically, the deliberate placement of an interface, which can readily open or shear, in front of a matrix crack, may blunt the crack by dispersing the large near-tip stress over the interface. This interfacial failure mode is desirable in terms of toughening, yet needs to compete against the mode of uninterrupted crack growth into the reinforcement. Thus, enormous attention has been dedicated to identifying the condition for enabling the interfacial failure mode while suppressing the undesirable crack penetration [19–40]. Interestingly, no consensus has been reached so far, primarily due to the wide variety of ways in which this problem has been formulated, as summarized in Table 1. Besides some minor differences in the model geometry, the major controversy revolves around the fracture criteria for the reinforcement and the interface. For example, Cook and Gordon [19] assumed that it is the cleavage stress, σ_i, generated by the approaching matrix crack at the interface (i.e., the tensile stress perpendicular to the interface) against the corresponding interfacial strength, $\sigma_{i,m}$, that governs the fracture of the interface; similarly, it is the splitting stress, σ_r, in the reinforcement (i.e., the tensile stress perpendicular to the matrix crack plane) against the corresponding strength, $\sigma_{r,m}$, that governs the fracture of the reinforcement. According to these assumptions, they concluded that the interfacial failure mode will be activated if σ_i reaches $\sigma_{i,m}$ before σ_r rises to $\sigma_{r,m}$. By contrast, He et al. [28–30,32] examined the energetic driving force (i.e., energy release rate) for extending an infinitesimal crack at the interface, G_i, and that for an infinitesimal crack growth in the reinforcement, G_r. They proposed an energy-based condition for triggering the interfacial failure mode, namely, G_i reaches the interfacial toughness, Γ_i, before G_r rises to the reinforcement's toughness, Γ_r. In addition, Parmigiani and Thouless [27] attempted to reconcile the above two types of fracture criteria by assuming that the failure of the interface and the reinforcement are both governed by cohesive laws.

While the different models listed in Table 1 address important aspects of failure in fiber-reinforced composites, there are several factors that have not been taken into consideration and can potentially affect the operative failure modes in these composites. First, finite-sized defects are commonly present [20], but most of the existing models assume that the interface and the reinforcement contain either no defects or infinitesimally small defects. Such assumptions might lead to unphysical interpretations such as unbounded or vanishing energetic driving forces for fracture initiation. Second, the residual stress generated during fabrication alters the stress state at the interface but has not drawn much attention. For example, the initiation of mode I fracture at the interface (e.g., interfacial delamination) might be suppressed if substantial compressive residual stresses act on the interface.

So far, we have only discussed the initiation of the favorable interfacial failure mode in a fiber-reinforced composite, as the matrix/reinforcement interface promises to dissipate appreciably more energy than the brittle reinforcement itself. However, the interfacial failure mode might be interrupted during the post-initiation process if the reinforcement is fractured or completely detached from the matrix. Therefore, a full description of interfacial failure from its initiation to termination is required to properly estimate the energy dissipation capacity of each individual matrix/reinforcement interface. Moreover, when quantifying the enhancement of the overall fracture toughness, we need to extend our consideration of these unit interfacial processes to the collective behavior of all the reinforcements and interfaces involved.

As summarized by Kelly [8], the interfacial failure mode exhibits two characteristic processes: interfacial debonding followed by frictional pull-out of the reinforcement along the interface. The debonding process dissipates energy through bond breaking between the reinforcement and matrix while the subsequent pull-out process dissipates energy through frictional sliding at the interface. In this regard, Kelly suggested a critical length, l_c, of the fiber reinforcement, which if not exceeded the reinforcement will not break and the interfacial failure mode will remain uninterrupted until complete pull-out. His further analysis suggested that l_c is roughly proportional to the ratio of the reinforcement's fracture strength, $\sigma_{r,m}$, to the interfacial frictional stress, τ_f. This critical length, l_c, sets an upper bound on the debonding energy dissipation, W_d, as well as on the energy dissipation during the pull-out process, W_p, for an individual interface. It is commonly believed that W_p is much greater than W_d, i.e., the energy dissipation capacity of the interface, W, should be mostly ascribed to the frictional pull-out process [8]. However, it is still unclear whether this argument holds when the reinforcements are downsized.

To bridge the gap between the toughening effect of each individual interface and that of an assembly of fibers, Kelly [8] assumed that each fiber fractures independently and exhibits identical properties, and thus calculated the work of fracture per unit area of the composite by multiplying each fiber's contribution and the area density of fibers. Curtin [41] further generalized Kelly's results by taking the statistical nature of composites into account. Note that the work of fracture, though not strictly equivalent to fracture toughness, has been considered as a reasonable measure of the resistance to fracture. Direct prediction of the enhanced fracture toughness of composites requires more sophisticated models such as the
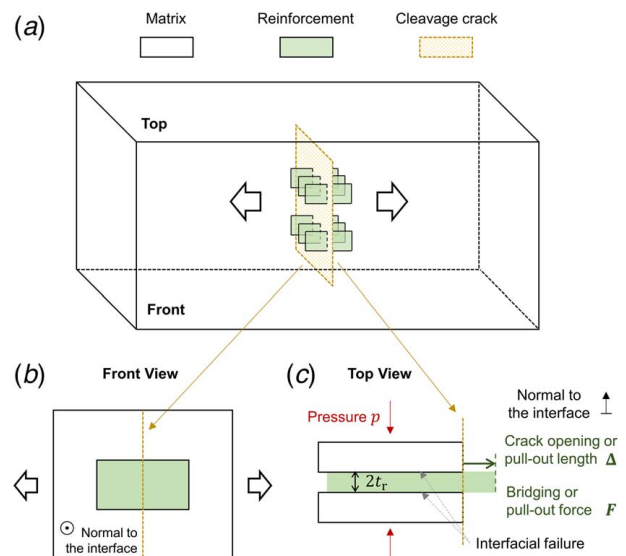
Fig. 1 Fracture of a 2D nanomaterial-reinforced composite. (a) A typical scenario of a cleavage crack being bridged by distributed platelet-like nano-reinforcements is considered in this work. (b) Each reinforcement is assumed to behave independently, leading to the reduced 2D model in (c). The increase in crack opening, Δ, arising from the subsequent loading drives the extraction of the reinforcement from the matrix and hence the interfacial failure process.
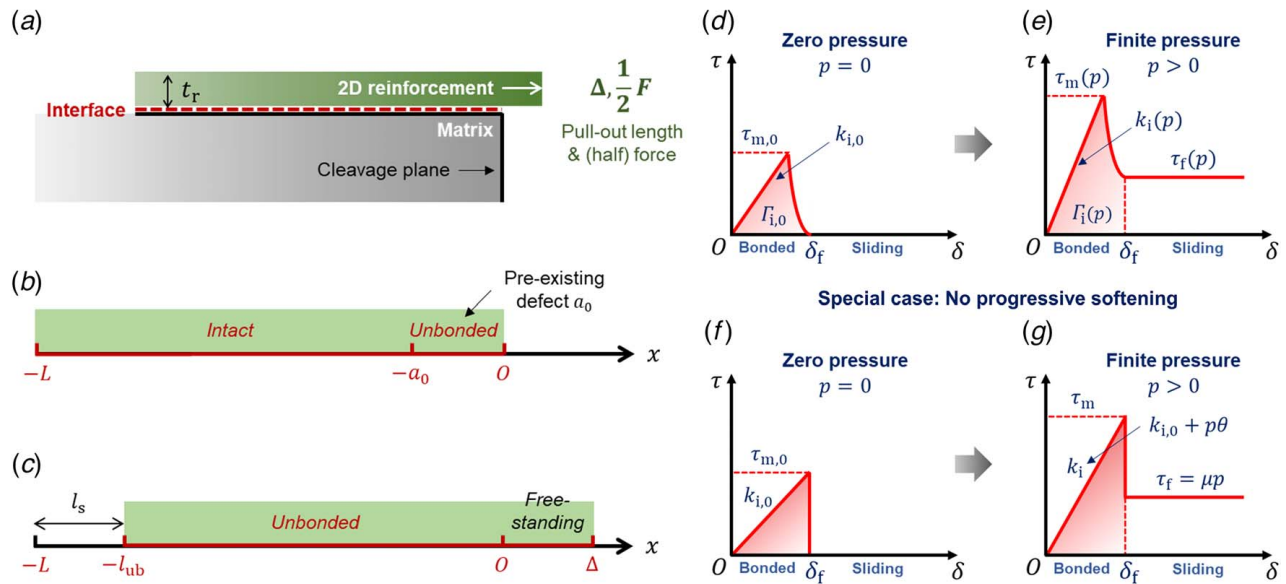
Fig. 2 A cohesive-frictional shear-lag model. (*a*) The half-reinforcement model accounts for one interface between the reinforcement and the matrix. Failure of the corresponding matrix/reinforcement interface is driven by the pull-out length, Δ, and the pull-out force, *F*. (*b*) Initial configuration of the interface. (*c*) Complete debonding of the interface followed by the pull-out process. (*d–g*) An extended cohesive model, with the Coulomb friction model embedded, is employed to describe the pressure-dependent sliding responses between the matrix and the reinforcement.

discontinuous crack-bridging model [42]. For simplicity, we will adopt the work-of-fracture method for estimating the overall fracture toughness of composites.

2.2 Toughening in 2D Nanomaterial-Reinforced Composites. Through revisiting the toughening mechanism in fiber-reinforced composites, we find that the existing theoretical and computational models are far from complete. The interfacial failure process, from its initiation to propagation (i.e., debonding and pull-out) to termination, remains elusive. These issues persist if we simply apply the existing models to the 2D nanomaterial-reinforced composites. Thus, it is necessary to build an extended model to capture the entire interfacial failure process.

It is important to note that in most cases nano-reinforcements are sparsely dispersed in the matrix and cannot form a sufficiently dense wall to block a matrix crack from traversing the composite. Thus, a typical scenario in a loaded composite is a scarcely opened cleavage crack being bridged by multiple platelet-like nano-reinforcements (Fig. 1(*a*)). Each of these platelets is circumvented by the cleavage surfaces. Moreover, as a result of the sparse dispersion, Kelly's assumption that each reinforcement behaves independently still stands as a reasonable approximation (Fig. 1(*b*)), thus leading to a reduced 2D model in Fig. 1(*c*). The increase in crack opening, Δ, arising from subsequent loading, drives the relative interfacial displacement between the matrix and the reinforcement (see Fig. 1(*c*) and the half model in Fig. 2(*a*)). For simplicity, we assume a pre-existing defect, i.e., an unbonded segment of size a_0, lying adjacent to the cleavage crack at the interface while the remaining part of the interface is initially intact (Fig. 2(*b*)). As Δ increases, the frictional force, τ_f, ramps up in the unbonded region and retards the initiation of debonding in the bonded region; the subsequent debonding is accompanied by a redistribution of interfacial shear stress, τ. Eventually, the whole interface can be completely unbonded and only subjected to friction if the strength of reinforcement is sufficiently high (Fig. 2(*c*)). In general, the frictional force, τ_f, should depend on the pressure exerted on the interface, p. A linear Coulomb model is assumed, $\tau_f = \mu p$, where μ is the coefficient of friction. In addition, the pressure is assumed to be uniformly distributed and can sufficiently

suppress interfacial delamination and ensure good contact between the matrix and the reinforcement. Note that the distribution of interfacial shear stress largely depends on the mechanical properties of the bond between the matrix and the reinforcement. A cohesive model can be used to characterize the bonding properties, revealing how the shear stress, τ, correlates with the relative displacement, δ, at the interface (Figs. 2(*d*)–2(*g*)). The interfacial bonding is typically achieved through a combination of chemical (e.g., covalent bond, hydrogen bond, dangling bond) and mechanical means (e.g., mechanical locking due to surface roughness) [43]. This complex mechanism of interfacial bonding, along with variable interfacial pressure, results in a wide range of interfacial stiffness, k_i, interfacial strength, τ_m, interfacial debonding length, δ_f, interfacial fracture energy, Γ_i, and frictional force, τ_f (Figs. 2(*d*) and 2(*e*)). Zhang et al. [44] conducted micron-scale *in situ* pull-out experiments to measure the unpressurized interfacial properties between a hexagonal boron nitride nanosheet (h-BN) and a polymer-derived ceramic (PDC) substrate, giving $k_{i,0} \approx 5.7$ GPa/μm, $\tau_{m,0} \approx 66.4$ MPa, $\delta_f \approx \tau_{m,0}/k_{i,0}$, and $\Gamma_{i,0} \approx 0.5\tau_m\delta_f$. Putra et al. [43] performed millimeter-scale push-out experiments and measured the properties of the graphite/epoxy interface, and reported $k_i \approx 0.2$ MPa/μm and $\tau_m \approx 1$–7 MPa. Adawi et al. [45–47] characterized the interface between a concrete slab and a cast-in-place concrete topping through meter-scale push-off experiments, giving $k_i \approx 3$–19 kPa/μm and $\tau_m \approx 0.2$ MPa. These measurements indicate a multi-scale character of interfacial bonding in composite materials. Since the length-scale of the h-BN/PDC experiments is most relevant to that in 2D nanomaterial-reinforced composites, e.g., the interfacial length and the interfacial shearing distance, we build an extended cohesive model (Figs. 2(*f*) and 2(*g*)) based on the h-BN/PDC data for characterizing the interfacial failure process. This cohesive model features a linear τ–δ response with a pressure-dependent stiffness, $k_i = k_{i,0} + p\theta$, a subsequent abrupt debonding at $\delta = \delta_f$, and the eventual frictional sliding governed by $\tau_f = \mu p$. As a result, the shear strength is pressure-dependent as well, $\tau_m = \tau_{m,0} + p\theta\delta_f$. Note that the h-BN/PDC data and the extended model do not exhibit a progressive softening regime after τ reaches τ_m, but it may generally exist (Figs. 2(*d*) and 2(*e*)). Moreover, this extended model, though has not been used in the studies of composites, bears some similarity to the slip-weakening model in the field of earthquake mechanics [48].

Based on the above cohesive-frictional model, the interfacial failure process is characterized by solving a well-defined shear-lag problem (Fig. 2). Specifically, the length of the interface under consideration, L, is one half the length of the corresponding reinforcement. Since the Young's moduli of the matrix and the 2D reinforcements are usually within the same order of magnitude and the reinforcements are much thinner than their spacings, we can reasonably focus on the deformation of the reinforcement along its pull-out direction, i.e., x-direction in Fig. 2, and assume the matrix is rigid. In this regard, the strain and stress distributions in the reinforcement are approximately uniform throughout the thickness. Due to the limited stretchability of the brittle reinforcement, small strains are assumed. However, the relative displacement at the interface may not be necessarily small, especially in the sliding part. The relative displacement field, $u(x)$, and stress field, $\sigma(x)$, in the deformed reinforcement along the x-direction are connected through

$$\sigma = E_r \, du/dx \tag{1}$$

where E_r is the modulus of the 2D reinforcement. The interfacial shear stress results in a gradient in σ:

$$d\sigma/dx = \tau/t_r \tag{2}$$

where t_r is the half-thickness of the 2D reinforcement. Both $u(x)$ and $\sigma(x)$ are defined in the deformed configuration. Combining Eqs. (1) and (2) gives

$$d^2u/dx^2 = \tau/(Et_r) \tag{3}$$

As the pull-out length Δ increases, the length of the contact interface decreases by l_s (the initial length is L). Accordingly, the left end of the reinforcement moves by $u(l_s - L) = l_s$, and the stress-free condition gives $\sigma(l_s - L) = 0$.

Before complete debonding, the interface consists of an unbonded/sliding region $(-l_{ub} < x < 0)$ of length l_{ub}, a bonded region $(l_s - L < x < -l_{ub})$ of length $l_b = L - l_s - l_{ub}$, and a free-standing region $(0 < x < \Delta)$ of length Δ. The expanding unbonded region maintains a relative displacement of δ_f at $x = -l_{ub}$: $u(-l_{ub}) = \delta_f$. According to the cohesive-frictional law in Fig. 2(g), the distribution of interfacial shear stress follows

$$\tau = \begin{cases} k_i u, & l_s - L \leq x < -l_{ub} \\ \tau_f, & -l_{ub} \leq x < 0 \\ 0, & 0 \leq x \leq \Delta \end{cases} \tag{4}$$

Substituting Eq. (4) into Eq. (3) gives a piecewise governing equation:

$$d^2u/dx^2 = \begin{cases} u/l_0^2, & l_s - L \leq x < -l_{ub} \\ \tau_f/(Et_r), & -l_{ub} \leq x < 0 \\ 0, & 0 \leq x \leq \Delta \end{cases} \tag{5}$$

where $l_0 = \sqrt{E_r t_r/k_i}$ is a characteristic length, measuring how locally the interfacial shear stress is distributed in the bonded part of the interface. In other words, it estimates the size of the "process zone" (PZ) of debonding within which the interfacial bonds are significantly more deformed than elsewhere. The PZ size increases with the stiffness of the reinforcement while decreasing with the interfacial stiffness. The differential equation in Eq. (5) can be solved by considering the abovementioned boundary conditions and the continuity conditions for displacement and stress. For $l_s - L \leq x \leq -l_{ub}$, we have

$$u = \delta_f \frac{\cosh[(x + L - l_s)/l_0]}{\cosh(l_b/l_0)} \tag{6}$$

The displacement at the left end of the bonded region is $l_s = \delta_f \text{sech}(l_b/l_0) \leq \delta_f$, thus l_b and l_{ub} are correlated by

$$l_{ub} = L - l_b - \delta_f \text{sech} \frac{l_b}{l_0} \tag{7}$$

The stress at the intersection of the bonded and unboned regions can be evaluated using Eq. (1), giving

$$\sigma(-l_{ub}) = \frac{E_r \delta_f}{l_0} \tanh \frac{l_b}{l_0} \tag{8}$$

For $-l_{ub} \leq x \leq 0$, we have

$$u = \delta_f + \frac{\tau_f}{2k_i l_0^2}(x + l_{ub})\left(x + l_{ub} + l_0 \frac{2\tau_m}{\tau_f} \tanh \frac{l_b}{l_0}\right) \tag{9}$$

The original length of the free-standing part of the reinforcement $(0 \leq x \leq \Delta)$ is exactly the displacement at $x = 0$:

$$u(0) = \delta_f + \frac{\tau_f}{2k_i l_0^2} l_{ub}\left(l_{ub} + l_0 \frac{2\tau_m}{\tau_f} \tanh \frac{l_b}{l_0}\right) \tag{10}$$

The constant stress in the free-standing part is also equal to that at the intersection of the free-standing and unbonded regions:

$$\sigma = \sigma(0) = \frac{E_r}{k_i l_0^2}\left(\tau_f l_{ub} + \tau_m l_0 \tanh \frac{l_b}{l_0}\right) \tag{11}$$

stretching the reinforcement by σ/E_r. Therefore, a semi-analytical solution to the pull-out length, Δ, and force, F, is obtained:

$$\begin{aligned} \Delta &= u(0)\left(1 + \frac{\sigma(0)}{E_r}\right) \\ &= \left(\frac{\tau_f l_{ub}^2}{2k_i l_0^2} + \frac{\delta_f l_{ub}}{l_0} \tanh \frac{l_b}{l_0} + \delta_f\right)\left(1 + \frac{\tau_f l_{ub}}{k_i l_0^2} + \frac{\delta_f}{l_0} \tanh \frac{l_b}{l_0}\right) \end{aligned} \tag{12}$$

$$F = \sigma(0) \cdot w_r \cdot 2t_r = 2w_r\left[\tau_f l_{ub} + \tau_m l_0 \tanh \frac{l_b}{l_0}\right] \tag{13}$$

where w_r is the width of the 2D reinforcement (in the out-of-plane direction of the shear-lag model). The prefactor of two in Eq. (13) accounts for the fact that the reinforcement is loaded on both sides (see Figs. 1(c) and 2(a)). By replacing l_{ub} in Eq. (13) with $l_{ub} = a_0 - \delta_f$, we can readily obtain the critical pull-out force, F_{init}, for initiating the debonding process from a defect of size a_0.

It should be noted that the analyzed debonding process refers to the entire process from the initial failure of the most stretched bond to the complete failure of all the bonds present at the interface. Therefore, it may not necessarily be a pure debonding process, rather a combination of debonding (in the bonded region) and frictional sliding (in the unbounded region). Strictly speaking, these two physically distinct processes are strongly coupled and should not be separately considered as in previous studies [8].

In contrast to the complex debonding process, the subsequent pull-out process relies solely on the operation of frictional sliding. Thus, the pull-out force, F, is proportional to the length of the contact interface, $l_{ub} = L - l_s$, and decreases monotonically with Δ until $\Delta = L$:
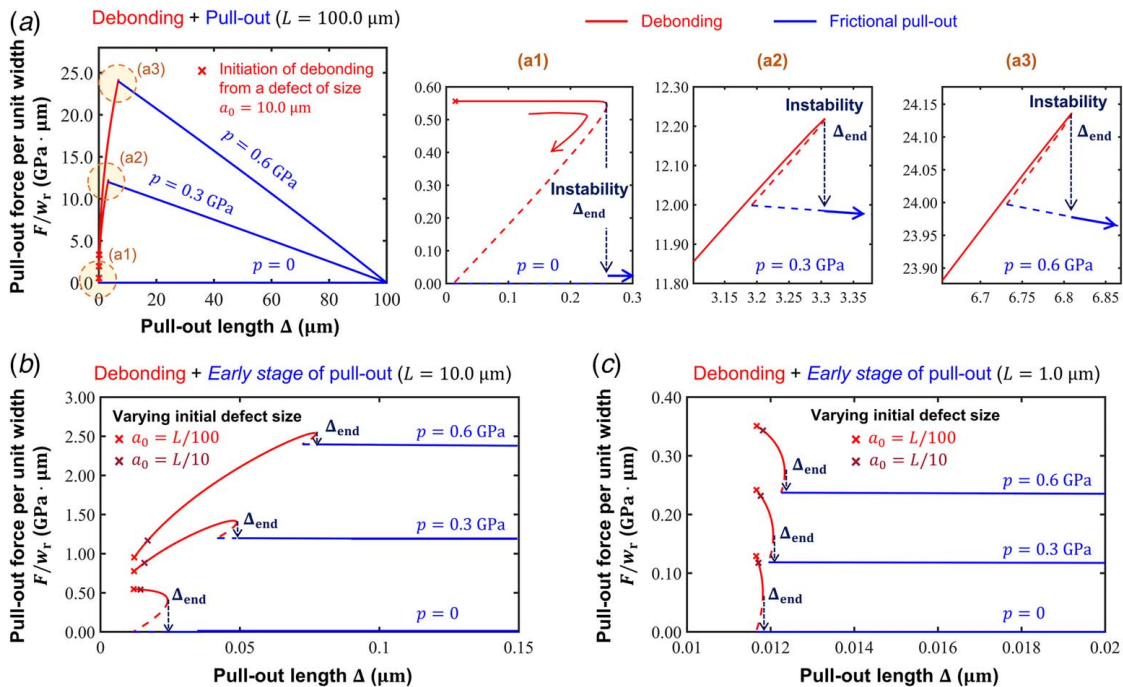
$$F = 2w_r \tau_f l_{ub} \tag{14}$$

In the absence of a bonded region, the interfacial displacement field is governed by

$$d^2u/dx^2 = \begin{cases} \tau_f/(Et_r), & -l_{ub} \leq x < 0 \\ 0, & 0 \leq x \leq \Delta \end{cases} \tag{15}$$

For $-l_{ub} \leq x \leq 0$, we have

$$u = \frac{\tau_f}{2k_i l_0^2}(x + l_{ub})^2 + L - l_{ub}, \quad \sigma = \frac{\tau_f}{k_i l_0^2}(x + l_{ub}) \tag{16}$$

satisfying the stress-free condition at $x = L - l_{ub}$. Thus, the pull-out length can be derived in a similar way as Eq. (12):

Fig. 3 Evolution of the pull-out force during the interfacial failure process. Both the debonding process and the pull-out process are accounted for. (a) The complete evolution of F from the initiation of debonding to the end of the pull-out process in the case of L = 100 μm. The insets (a1–a3) zoom into the transition from debonding to frictional pull-out for p = 0, 0.3 GPa, and 0.6 GPa, respectively, revealing a universal "snap-back" instability (marked in dashed arrows). ((b) and (c)) A zoom-in view of the evolution of F during the debonding process and the early stage of the pull-out process for L = 10 μm and L = 1 μm.

Table 2   Model parameters used in this work

| E_r (GPa)	t_r (μm)	$\tau_{m,0}$ (MPa)	$k_{i,0}$ (GPa/μm)	δ_f (μm)
500.0	0.2	66.4	5.7	0.0116
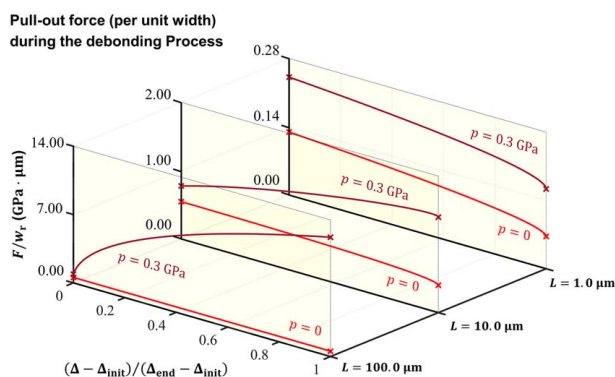
Fig. 4 Evolution of the pull-out force during the debonding process. Significant variations of F/w_r with respect to p and L are observed. The maximum pull-out force can be reached in the beginning, the middle, or the end of the debonding process due to different combinations of p and L.

$$\Delta = u(0)\left(1 + \frac{\sigma(0)}{E_r}\right) = \left(\frac{\tau_f l_{ub}^2}{2 k_i l_0^2} + L - l_{ub}\right)\left(1 + \frac{\tau_f l_{ub}}{k_i l_0^2}\right) \quad (17)$$

Figure 3(a) shows how F and Δ evolve as the interfacial failure proceeds under different pressures, assuming $\mu = \theta \delta_f = 0.2$, the initial length of the interface is $L = 100.0\,\mu$m, and the interface

contains a pre-existing defect of size $a_0 = 10.0\,\mu$m. All the other parameters are listed in Table 2. The F–Δ curve in Fig. 3(a) and its insets outline the transition from debonding to pure frictional pull-out (the long tail). In the absence of pressure and friction, only the debonding process gives a nonzero F. The F–Δ curve prior to the initiation of debonding is not plotted since it follows a simple linear relationship. Figures 3(b) and 3(c) zoom into the debonding process and the early stage of the frictional pull-out process, showing significant variation for different L and p. The initiation point (marked with crosses), F_{init} and Δ_{init}, is sensitive to the initial defect size, a_0, thus revealing the critical role of pre-existing defects in initiating the debonding process. Interestingly, the subsequent evolution of F and Δ falls onto one master curve that is insensitive to a_0. One prominent feature of these F–Δ curves is the "snap-back" instability (see the dashed arrows in Figs. 3(b) and 3(c) and the insets of Fig. 3(a)) at the end of the debonding process, $\Delta = \Delta_{end}$, upon which only if F and Δ decrease simultaneously, debonding can proceed in a quasi-static manner. The decrease in F accommodates the loss in the load-carrying capability of the interface due to its shrinking and debonding, while the decrease in Δ arises from the accompanying elastic recovery of the stretched reinforcement. Generally, in a monotonically loaded system, the instability point will be bypassed, such that the interface will become completely unbonded when Δ exceeds Δ_{end}, and switch to pure sliding. In other words, the "snap-back" instability causes immediate termination of the debonding process and initiation of the pull-out process.

Figure 4 reveals the detailed evolution of F during the debonding process by plotting F against a normalized coordinate $(\Delta - \Delta_{init})/(\Delta_{end} - \Delta_{init})$. From Fig. 4, we note that the pressure-free scenarios ($p = 0$ and $a_0 = L/100$) are exclusively indicative of a size effect associated with L. Immediately after the initiation of debonding ($\Delta = \Delta_{init}$), the pull-out force, F, exhibits a plateau in the case of a long interface ($L = 100.0\,\mu$m) while decreasing more drastically for shorter interfaces ($L = 1.0$ and $10.0\,\mu$m). Such transition, as discussed in Ref. [44], is governed by the PZ size, l_0 (see Eq. (5)). For
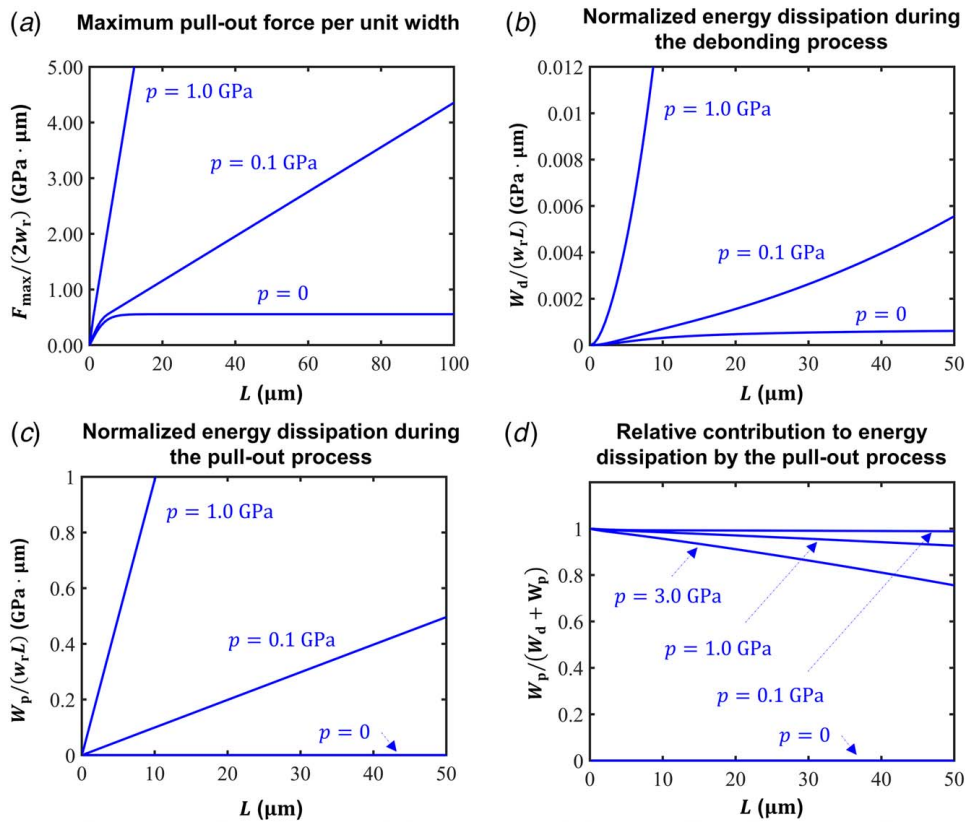
Fig. 5   Key characteristic quantities of the interfacial failure process. (a) The maximum pull-out force during the entire interfacial failure process. (b) The amount of energy dissipated by the debonding process. (c) The amount of energy dissipated by the pull-out process. (d) The relative contribution to energy dissipation by the pull-out process.

all the curves in Fig. 4, $l_0 = 2.5$ μm if $p = 0$. In this regard, debonding of a long interface ($L \gg l_0$) essentially involves mode II cracking with a highly localized crack front (i.e., PZ), resulting in an almost constant pull-out force as the crack front moves and the bonded region shrinks. By contrast, a short interface ($L \approx l_0$ or $L < l_0$) undergoes more dispersedly distributed shear stress in the bonded region, making F more susceptible to the change in the length of the bonded region. The difference between these two modes is also reflected in the maximum pull-out force, F_{max}. In the pressure-free case (Fig. 5(a)), F_{max} increases almost linearly with L when L is small. This is because the interfacial shear stress is roughly uniformly distributed ($\tau \approx \tau_m$) and F_{max} is limited by both τ_m and L (i.e., the so-called strength-governed limit [44]). However, F_{max} becomes saturated when $L \gg l_0$ as debonding of a long interface is essentially an energetic fracture process that can be driven by a constant F (i.e., the so-called energy-governed limit [44]).

From Fig. 4, we also note that for the case of finite pressures ($p > 0$ and $a_0 = L/100$), additional complexities are introduced to the debonding process. The plateau of F for $L \gg l_0$ in the pressure-free case no longer exists for finite pressures, and F may even increase during debonding due to the presence of friction. Therefore, F_{max} is not necessarily equal to F_{init} and can probably be reached in the middle or the end of the debonding process. The pressure effect is more pronounced for a long interface, in which case F_{max} (roughly proportional to L) mainly arises from friction rather than interfacial bonding (Fig. 5(a)).

Figures 5(b) and 5(c) show how the amount of energy dissipated by an interface during the debonding process, W_d, and the pull-out process, W_p, vary with L and p. Note that W_d can be readily evaluated by taking the integral of $F/2$ from Δ_{init} to Δ_{end} while W_p by the integral of $F/2$ from Δ_{end} to L. For all the curves in Fig. 5, a small defect size is assumed: $a_0 = L/100$. It is found that W_p increases linearly with L, but the W_d–L relationship is rather complex and cannot

be described by a simple power law as it was in Kelly's analysis [8]. In order to understand the relative contributions to energy dissipation by the debonding and pull-out processes, we plot the ratio of W_d to W ($= W_d + W_p$) for various L and p in Fig. 5(d). In contrast to the prevailing view that $W \approx W_p$, a substantial energy can be dissipated through the debonding process. Such deviation is not specific to the pressure-free case in which $W_p = 0$ and $W_d > 0$. For large p and L, W_d can also be comparable to W_p, which is essentially caused by the forementioned fact that W_d arises from coupled debonding in the bonded region and frictional sliding in the unbounded region. As p increases from 0.1 GPa to 3.0 GPa (see the curves in Fig. 5(d)), the relative contribution from W_d increases. This results from the prolonged debonding process and the correspondingly shortened pull-out process, as manifested in Fig. 3 by an increasing Δ_{end}/L with p.

Intuitively, the energy dissipation capacity of an interface should be comparable to $\tilde{W} = \tau_f L^2/2 + \Gamma_i L$, which is the sum of the energy dissipation by an unbounded interface of a rigid reinforcement and that by a bonded but frictionless interface of a rigid reinforcement. Thus, we plot the ratio of W to $\tilde{W}$ against L for a wide range of pressures in Fig. 6(a). Interestingly, all these curves monotonically increase with L while exhibiting a nonmonotonic dependence on p. A significant discrepancy between W and $\tilde{W}$ is observed for small L, indicating that short reinforcements might not be optimal in terms of their potential to dissipate energy if the size-induced variations in their mechanical properties are excluded. Moreover, since $\tilde{W}$ increases with p, a larger pressure should be able to enhance the energy dissipation capacity of the reinforcements, W. However, there is still one limiting factor for fulfilling their toughening potential, i.e., the failure of the reinforcements themselves, which has certainly drawn numerous research interest yet exceeds the scope of this work [49,50]. Here, for simplicity, we assume an effective strength, S,
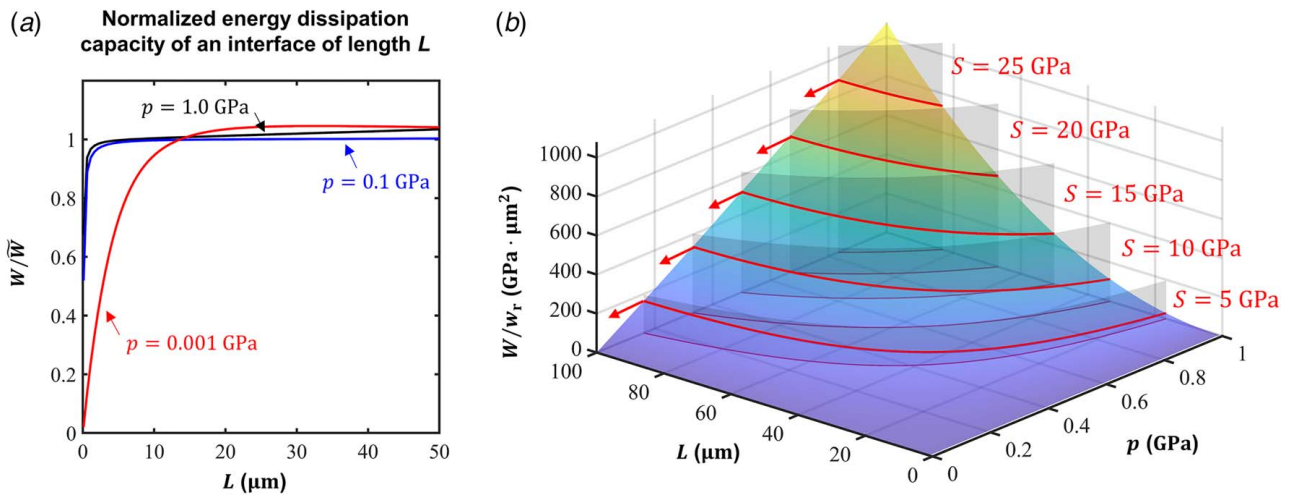
Fig. 6 Utilizing the full energy dissipation capacity of the matrix/reinforcement interface. (a) A long interface and a large pressure can generally enhance the energy dissipation capacity. (b) The failure strength, S, of the reinforcement, however, limits the practical utilization of the dissipation capacity. The p–L regime, as enclosed by the gray walls and pointed towards by the arrows, defines the admissible design space that prevents the intermediate interruption of the interfacial failure process. The intersection line between the boundary of the admissible regime and the contour plot of W determines the optimal L for a given p, or an optimal p for a given L.

governing their failure. Thus, an uninterrupted dissipation process requires

$$F_{\max} \leq S \cdot 2t_r \qquad (18)$$

For a given S, Eq. (18) determines an "admissible" p–L regime, as enclosed by the gray walls, and pointed towards by the arrows in Fig. 6(b). By examining the intersection line between the boundary of the admissible regime and the contour plot of W, we can find an optimal/maximum L for a given p, or an optimal/maximum p for a given L (see the intersection lines in Fig. 6(b)). Though Fig. 6(b) depends on the choice of modeling parameters (Table 2), we can make a few general remarks as follows:

(1) It is favorable to combine a large L and a correspondingly small p on the intersection line. Although both large L and p can enhance W, the constraint in Eq. (18) poses a trade-off between them. Hence, it is more critical to increase L for gaining higher toughness.

(2) An upper bound of L (due to practical constraints such as fabrication) can lead to an optimal p, beyond which the toughening effects of reinforcements are diminished.

(3) Similarly, a lower bound of p determines an upper bound of L as a long interface is prone to fracture according to Eq. (18).

(4) A large S is always beneficial to toughening the composites. Thus, it is reasonable to take advantage of 2D nanomaterials in the design of composites as most of them are known for their high strengths.

3 Discussion and Concluding Remarks

In Sec. 2.2, we present a comprehensive model of the interfacial failure process and a detailed F–Δ curve (or equivalently, the relationship between the crack-bridging force and the crack opening displacement). This model separates energy dissipation between the debonding and pull-out processes, and highlights the effects of interfacial pressure, p, and the length of the interface, L. We identify two key characteristic quantities for the interfacial failure process: the maximum pull-out force, $F_{\max}$, and the total energy dissipation capacity of the interface, W. The admissible design space for p and L, within which the interfacial failure process will initiate and proceed without interruption (Eq. (18)), is determined by $F_{\max}$ and the strength of the reinforcement, S. This constraint is stronger

than merely limiting the critical force for enabling interfacial failure, F_{init}, to S, as $F_{\max} \geq F_{\text{init}}$ (see Fig. 4). Thus, ensuring an uninterrupted interfacial failure mode in composites is a more practically relevant problem compared to the extensively studied crack deflection problem in the literature (Table 1). Even in the strength-governed limit (i.e., the case of small L) where $F_{\max} = F_{\text{init}}$, the previous studies are incomplete as they largely neglected the sensitivity to pre-existing defects and pressure (Fig. 3(c)). It is important to note that practical situations may involve constraints that are not captured by Eq. (18), requiring consideration of all constraints to maximize W (Fig. 6(b)). Assuming n aligned bridging reinforcements (with length $2L$ and thickness $2t_r$) per unit area, the overall toughness increase of the composites can be roughly estimated as $4\,nW$, according to the work-of-fracture method. Therefore, optimizing the toughness and W are equivalent. It should be noted that the alignment of reinforcements renders the mechanical properties of the composites anisotropic [8], and in this work we focus on the toughening effects for one specific fracture mode/direction. The anisotropy of toughening can be particularly appealing in practical situations where the loading condition requires significantly higher toughening in one direction compared to the others.

The continuum analysis in this study does not predict a significant shift in the toughening mechanism with size. This result implies limited benefits associated with the use of 2D nanoreinforcements. While our theoretical framework is applicable to both micro- and nano-platelets, it is important to recognize that the parameters such as reinforcement stretchability and interfacial properties can exhibit a strong size-dependence. For example, the high strength of nanomaterials enables the use of longer reinforcements (i.e., a reinforcement material with larger L that does not undergo fracture). Additionally, the reduced thickness of 2D nano-platelets increases the number of the matrix/reinforcement interfaces (for a given volume fraction) and hence the overall toughness. Furthermore, each thin reinforcement may be within several atomic spacings of the interface, thus complicating the representation of bulk and interfacial properties in the continuum analysis as they are not readily measurable by experiments.

Our analysis is based on a cohesive-frictional law that is assumed to govern the debonding and frictional sliding of the matrix/reinforcement interface. Proper characterization of the interface, especially the pressure and size effects, is necessary for designing strong and tough CMCs in a specific material system. The unique layered structure of 2D nanomaterials also brings new opportunities

for tuning interfacial properties through engineered interfacial bonding and morphology. Moreover, the weak interaction between the internal layers of 2D nanomaterials might give rise to additional failure mechanisms such as the "sword-in-sheath" mode of crack bridging that has been observed with multiwalled carbon nanotubes [51]. Specifically, the failure process associated with debonding and pull-out might occur between the internal layers of nano-reinforcements rather than at the matrix/reinforcement interface. These two modes can contribute concurrently to toughening in ways that are associated with variations in the specific reinforcement structures and properties.

In practical situations, the source of pressure in the cohesive-frictional law must also be considered. In most composite materials, significant residual stresses are generated due to thermal expansion mismatch between the reinforcements and the matrix. Additionally, external loading can exert substantial pressure at the interface. This can potentially resemble the effect of T-stress [52,53] on the fracture of composites.

Acknowledgment

Conflict of Interest

There are no conflicts of interest.

Data Availability Statement

The authors attest that all data for this study are included in the paper.

References

[1] Gao, H., Ji, B., Jäger, I. L., Arzt, E., and Fratzl, P., 2003, "Materials Become Insensitive to Flaws at Nanoscale: Lessons From Nature," Proc. Natl. Acad. Sci. U.S.A., **100**(10), pp. 5597–5600.

[2] Ren, J., Zhang, Y., Zhao, D., Chen, Y., Guan, S., Liu, Y., Liu, L., et al., 2022, "Strong Yet Ductile Nanolamellar High-Entropy Alloys by Additive Manufacturing," Nature, **608**(7921), pp. 62–68.

[3] Xiao, S., Chen, C., Xia, Q., Liu, Y., Yao, Y., Chen, Q., Hartsfield, M., et al., 2021, "Lightweight, Strong, Moldable Wood Via Cell Wall Engineering as a Sustainable Structural Material," Science, **374**(6566), pp. 465–471.

[4] Athanasiou, C. E., Zhang, H., Ramirez, C., Xi, J., Baba, T., Wang, X., Zhang, W., Padture, N. P., Szlufarska, I., and Sheldon, B. W., 2020, "High Toughness Carbon-Nanotube-Reinforced Ceramics Via Ion-Beam Engineering of Interfaces," Carbon, **163**, pp. 169–177.

[5] Athanasiou, C. E., Jin, M. Y., Ramirez, C., Padture, N. P., and Sheldon, B. W., 2020, "High-Toughness Inorganic Solid Electrolytes Via the Use of Reduced Graphene Oxide," Matter, **3**(1), pp. 212–229.

[6] Padture, N. P., 2016, "Advanced Structural Ceramics in Aerospace Propulsion," Nat. Mater., **15**(8), pp. 804–809.

[7] Padture, N. P., 2019, "Environmental Degradation of High-Temperature Protective Coatings for Ceramic-Matrix Composites in Gas-Turbine Engines," NPJ Mater. Degrad., **3**(1), pp. 1–6.

[8] Kelly, A., 1970, "Interface Effects and the Work of Fracture of a Fibrous Composite," Proc. R. Soc. Lond. A Math. Phys. Sci., **319**(1536), pp. 95–116.

[9] Marshall, D. B., and Evans, A. G., 1985, "Failure Mechanisms in Ceramic-Fiber/Ceramic-Matrix Composites," J. Am. Ceram. Soc., **68**(5), pp. 225–231.

[10] Huang, L. J., Geng, L., and Peng, H. X., 2015, "Microstructurally Inhomogeneous Composites: Is a Homogeneous Reinforcement Distribution Optimal?," Prog. Mater. Sci., **71**, pp. 93–168.

[11] González, C., Vilatela, J. J., Molina-Aldareguía, J. M., Lopes, C. S., and Lorca, J., 2017, "Structural Composites for Multifunctional Applications: Current Challenges and Future Trends," Prog. Mater. Sci., **89**, pp. 194–251.

[12] Ramirez, C., Miranzo, P., Belmonte, M., Osendi, M. I., Poza, P., Vega-Diaz, S. M., and Terrones, M., 2014, "Extraordinary Toughening Enhancement and Flexural Strength in Si₃N₄ Composites Using Graphene Sheets," J. Eur. Ceram. Soc., **34**(2), pp. 161–169.

[13] Walker, L. S., Marotto, V. R., Rafiee, M. A., Koratkar, N., and Corral, E. L., 2011, "Toughening in Graphene Ceramic Composites," ACS Nano, **5**(4), pp. 3182–3190.

[14] Zhang, X., Zhao, N., and He, C., 2020, "The Superior Mechanical and Physical Properties of Nanocarbon Reinforced Bulk Composites Achieved by Architecture Design—A Review," Prog. Mater. Sci., **113**, p. 100672.

[15] Griffith, A. A., 1921, "The Phenomena of Rupture and Flow in Solids," Philos. Trans. R. Soc. Lond. Ser. A: Contain. Pap. Math. Phys. Charact., **4**(1), pp. 9–14.

[16] Irwin, G. R., 1957, "Analysis of Stresses and Strains Near the End of a Crack Traversing a Plate," ASME J. Appl. Mech., **24**(3), pp. 361–364.

[17] Rice, J. R., 1968, "A Path Independent Integral and the Approximate Analysis of Strain Concentration by Notches and Cracks," ASME J. Appl. Mech., **35**(2), pp. 379–386.

[18] Cottrell, A. H., 1965, "The Ultimate Mechanical Properties of Solids," Metall. Achieve., pp. 259–272.

[19] Cook, J., and Gordon, J. E., 1964, "A Mechanism for the Control of Crack Propagation in All-Brittle Systems," Proc. R. Soc. Lond. Ser. A: Math. Phys. Sci., **282**(1391), pp. 508–520.

[20] Lee, W., Howard, S. J., and Clegg, W. J., 1996, "Growth of Interface Defects and Its Effect on Crack Deflection and Toughening Criteria," Acta Mater., **44**(10), pp. 3905–3922.

[21] Tu, W.-C., Lange, F. F., and Evans, A. G., 1996, "Concept for a Damage-Tolerant Ceramic Composite With 'Strong' Interfaces," J. Am. Ceram. Soc., **79**(2), pp. 417–424.

[22] Ahn, B. K., Curtin, W. A., Parthasarathy, T. A., and Dutton, R. E., 1998, "Criteria for Crack Deflection/Penetration Criteria for Fiber-Reinforced Ceramic Matrix Composites," Compos. Sci. Technol., **58**(11), pp. 1775–1784.

[23] Leguillon, D., Lacroix, C., and Martin, E., 2000, "Interface Debonding Ahead of a Primary Crack," J. Mech. Phys. Solids, **48**(10), pp. 2137–2161.

[24] Roham, S., Hardikar, K., and Woytowitz, P., 2004, "Crack Penetration and Deflection at a Bimaterial Interface in a Four-Point Bend Test," J. Mater. Res., **19**(10), pp. 3019–3027.

[25] Lee, W., Yoo, Y. H., and Shin, H., 2004, "Reconsideration of Crack Deflection at Planar Interfaces in Layered Systems," Compos. Sci. Technol., **64**(15), pp. 2415–2423.

[26] Gupta, V., Argon, A. S., and Suo, Z., 1992, "Crack Deflection at an Interface Between Two Orthotopic Media," ASME J. Appl. Mech., **59**(2S), pp. S79–S87.

[27] Parmigiani, J. P., and Thouless, M. D., 2006, "The Roles of Toughness and Cohesive Strength on Crack Deflection at Interfaces," J. Mech. Phys. Solids, **54**(2), pp. 266–287.

[28] He, M.-Y., and Hutchinson, J. W., 1989, "Crack Deflection at an Interface Between Dissimilar Elastic Materials," Int. J. Solids Struct., **25**(9), pp. 1053–1067.

[29] He, M., Bartlett, A., Evans, A. G., and Hutchinson, J. W., 1991, "Kinking of a Crack Out of an Interface: Role of In-Plane Stress," J. Am. Ceram. Soc., **74**(4), pp. 767–771.

[30] He, M.-Y., Evans, A. G., and Hutchinson, J. W., 1994, "Crack Deflection at an Interface Between Dissimilar Elastic Materials: Role of Residual Stresses," Int. J. Solids Struct., **31**(24), pp. 3443–3455.

[31] Paggi, M., and Reinoso, J., 2017, "Revisiting the Problem of a Crack Impinging on an Interface: A Modeling Framework for the Interaction Between the Phase Field Approach for Brittle Fracture and the Interface Cohesive Zone Model," Comput. Methods Appl. Mech. Eng., **321**, pp. 145–172.

[32] He, M.-Y., Hsueh, C. H., and Becher, P. F., 2000, "Deflection Versus Penetration of a Wedge-Loaded Crack: Effects of Branch-Crack Length and Penetrated-Layer Width," Compos. Part B: Eng., **31**(4), pp. 299–308.

[33] Zhang, Z., and Suo, Z., 2007, "Split Singularities and the Competition Between Crack Penetration and Debond at a Bimaterial Interface," Int. J. Solids Struct., **44**(13), pp. 4559–4573.

[34] Martin, E., Leguillon, D., and Lacroix, C., 2001, "A Revisited Criterion for Crack Deflection at an Interface in a Brittle Bimaterial," Compos. Sci. Technol., **61**(12), pp. 1671–1679.

[35] Kendall, K., 1975, "Transition Between Cohesive and Interfacial Failure in a Laminate," Proc. R. Soc. Lond. A: Math. Phys. Sci., **344**(1637), pp. 287–302.

[36] Thouless, M. D., and Evans, A. G., 1988, "Effects of Pull-Out on the Mechanical Properties of Ceramic-Matrix Composites," Acta Metall., **36**(3), pp. 517–522.

[37] Ye, T., Suo, Z., and Evans, A. G., 1992, "Thin Film Cracking and the Roles of Substrate and Interface," Int. J. Solids Struct., **29**(21), pp. 2639–2648.

[38] Gupta, V., Yuan, J., and Martinez, D., 1993, "Calculation, Measurement, and Control of Interface Strength in Composites," J. Am. Ceram. Soc., **76**(2), pp. 305–315.

[39] Tullock, D. L., Reimanis, I. E., Graham, A. L., and Petrovic, J. J., 1994, "Deflection and Penetration of Cracks at an Interface Between Two Dissimilar Materials," Acta Metall. Mater., **42**(9), pp. 3245–3252.

[40] Martínez, D., and Gupta, V., 1994, "Energy Criterion for Crack Deflection at an Interface Between Two Orthotropic Media," J. Mech. Phys. Solids, **42**(8), pp. 1247–1271.

[41] Curtin, W. A., 1991, "Theory of Mechanical Properties of Ceramic-Matrix Composites," J. Am. Ceram. Soc., **74**(11), pp. 2837–2845.

[42] Shao, Y., Zhao, H. P., Feng, X. Q., and Gao, H., 2012, "Discontinuous Crack-Bridging Model for Fracture Toughness Analysis of Nacre," J. Mech. Phys. Solids, **60**(8), pp. 1400–1419.

[43] Putra, I. S., Budiman, B. A., Sambegoro, P. L., Santosa, S. P., Mahyuddin, A. I., Kishimoto, K., and Inaba, K., 2020, "The Influence of Fiber Surface Profile and Roughness to Fiber–Matrix Interfacial Properties," J. Compos. Mater., **54**(11), pp. 1441–1452.

[44] Zhang, B., Liu, X., Guo, H., Yang, K., Gao, G., Sheldon, B. W., Gao, H., and Lou, J., 2021, "Quantitative In-Situ Study of Strength-Governed Interfacial Failure Between h-BN and Polymer-Derived Ceramic," Acta Mater., **210**, p. 116832.

[45] Adawi, A., Youssef, M. A., and Meshaly, M., 2014, "Analytical Modeling of the Interface Between Lightly Roughened Hollowcore Slabs and Cast-In-Place Concrete Topping," J. Struct. Eng., **141**(4), p. 04014119.

[46] Adawi, A., Youssef, M. A., and Meshaly, M. E., 2015, "Experimental Investigation of the Composite Action Between Hollowcore Slabs With Machine-Cast Finish and Concrete Topping," Eng. Struct., **91**, pp. 1–15.

[47] Adawi, A., Youssef, M. A., and Meshaly, M. E., 2016, "Evaluating Interfacial Shear Stresses in Composite Hollowcore Slabs Using Analytical Solution," Alexandria Eng. J., **55**(3), pp. 2647–2654.

[48] Ida, Y., 1972, "Cohesive Force Across the Tip of a Longitudinal-Shear Crack and Griffith's Specific Surface Energy," J. Geophys. Res., **77**(20), pp. 3796–3805.

[49] Ni, B., Steinbach, D., Yang, Z., Lew, A., Zhang, B., Fang, Q., Buehler, M. J., and Lou, J., 2022, "Fracture at the Two-Dimensional Limit," MRS Bull., **47**(8), pp. 848–862.

[50] Zhang, P., Ma, L., Fan, F., Zeng, Z., Peng, C., Loya, P. E., Liu, Z., et al., 2014, "Fracture Toughness of Graphene," Nat. Commun., **5**(1), pp. 1–7.

[51] Liu, Y., Ramirez, C., Zhang, L., Wu, W., and Padture, N. P., 2017, "In Situ Direct Observation of Toughening in Isotropic Nanocomposites of Alumina Ceramic and Multiwall Carbon Nanotubes," Acta Mater., **127**, pp. 203–210.

[52] Cotterell, B., 1966, "Notes on the Paths and Stability of Cracks," Int. J. Fract. Mech., **2**(3), pp. 526–533.

[53] Cotterell, B., and Rice, J. R., 1980, "Slightly Curved or Kinked Cracks," Int. J. Fract., **16**(2), pp. 155–169.